Flame-Sprayed Superparamagnetic Bare and Silica-Coated Maghemite Nanoparticles: Synthesis, Characterization, and Protein Adsorption−Desorption

Dan Li,[†] Wey Yang Teoh,[†] Cordelia Selomulya,[‡] Robert C. Woodward,[§] Rose Amal,*[,†] and Bettina Rosche[||]

ARC Centre for Functional Nanomaterials, School of Chemical Sciences and Engineering, and School of Biotechnology & Biomolecular Sciences, The University of New South Wales, Sydney NSW 2052 Australia, Department of Chemical Engineering, Clayton Campus, Monash University, Melbourne VIC 3800 Australia, and School of Physics, M013, The University of Western Australia, Crawley WA 6009 Australia

Received August 7, 2006. Revised Manuscript Received October 14, 2006

Superparamagnetic maghemite (γ-Fe_2O_3) nanoparticles of tunable diameters and silica-coated maghemite (SiO_2/γ-Fe_2O_3) nanoparticles of controllable morphology were successfully synthesized using a one-step flame spray pyrolysis (FSP) technique. The physical, chemical, and magnetic properties of γ-Fe_2O_3 and SiO_2/γ-Fe_2O_3 nanostructures were characterized and compared with those of silica-coated FSP γ-Fe_2O_3 produced by a conventional sol−gel method. Bovine serum albumin (BSA) adsorption−desorption was investigated as a model to demonstrate the feasibility of synthesized superparamagnetic nanoparticles for bioadsorption and bioseparation. Protein adsorption was observed to follow the Langmuir isotherm, with the highest binding capacity of 348 mg of BSA/g of particle and a dissociation constant of 0.0159 g/L attainable for FSP γ-Fe_2O_3 (d_{XRD} = 14 nm) in 10 mM formate buffer. Electrostatically governed BSA orientations were proposed for different particle−buffer systems. Shifting the pH of suspension with K_2HPO_4 enabled effective recovery of adsorbed BSA.

1. Introduction

The application of magnetic particles in the field of biological and biomedical science can be traced back to the 1970s, when micron-sized particles were used as support materials for enzyme immobilization[1] and bioaffinity adsorbents.[2] Success in synthesizing magnetic particles in the nanosize range is revolutionizing a wide range of in vivo and in vitro bioapplications,[3,4] including magnetic resonance imaging (MRI),[5] biosensors,[6] bioseparation and enzyme immobilization,[7−10] DNA capturing, cancer therapy,[11,12] and targeted drug delivery.[13,14] Particles in the nanosize range possess distinctively different physiochemical, magnetic, and optical properties compared to their bulk phase. An example of these unique properties is superparamagnetism, which for magnetite and maghemite particles at room temperature is observed for particles with a size below 20 nm.[15] This particular magnetic characteristic is extremely desirable for bioapplications, as it avoids magnetically induced self-aggregation of the particles that tends to alter the functionality/performance of the system.[15] Regardless of the diversity in applications, the ideal magnetic nanostructures for bioapplications would have these desirable properties, i.e., uniform size, high surface area, fast adsorption kinetics, biocompatibility, as well as superparamagnetism with high magnetic strength. Often, an additional inorganic or polymeric coating layer is necessary to avoid magnetically induced self-aggregation of magnetic cores and to improve the functionality or biocompatibility of these nanostructures.

The characteristic of protein adsorption−desorption on surfaces of magnetic particles is of particular importance as it reflects the interaction between synthetic materials and the biomolecule of interest. Besides mimicking some of the in vivo processes like drug delivery, the adsorption−desorption of protein is also a key reaction step in many bioprocesses found in the food and pharmaceutical industries. Traditional bioseparation relies on the RIPP (removal, isolation, purifica-

* Corresponding author: Tel.: +61 2 9385 4361. Fax: +61 2 9385 5966. E-mail: r.amal@unsw.edu.au.

[†] ARC Centre for Functional Nanomaterials, The University of New South Wales.

[‡] Monash University.

[§] The University of Western Australia.

[||] School of Biotechnology & Biomolecular Sciences, The University of New South Wales.

(1) Robinson, P. J.; Dunnill, P.; Lilly, M. D. *Biotechnol. Bioeng.* **1973**, *15*, 603.
(2) Dunnill, P.; Lilly, M. D. *Biotechnol. Bioeng.* **1974**, *16*, 987.
(3) Pankhurst, Q. A.; Connolly, J.; Jones, S. K.; Dobson, J. *J. Phys. D: Appl. Phys.* **2003**, *36*, R167.
(4) Safarik, I.; Safarikova, M. *Biomagn. Res. Technol.* **2004**, *2*:7.
(5) Bomatí-Miguel, O.; Morales, M. P.; Tartaj, P.; Ruiz-Cabello, J.; Bonville, P.; Santos, M.; Zhao, X.; Veintemillas-Verdaguer, S. *Biomaterials* **2005**, *26*, 5695.
(6) Josephson, L.; Perez, J. M.; Weissleder, R. *Angew. Chem. Int. Ed.* **2001**, *40*, 3204.
(7) Bucak, S.; Jones, D. A.; Laibinis, P. E.; Hatton, T. A. *Biotechnol. Prog.* **2003**, *19*, 477.
(8) Heebøll-Nielsen, A.; Dalkiær, M.; Hubbuch, J. J.; Thomas, O. R. T. *Biotechnol. Bioeng.* **2004**, *87* (3), 311.
(9) Guo, Z.; Sun, Y.; *Biotechnol. Prog.* **2004**, *20*, 500.
(10) Huang, S. H; Liao, M. H.; Chen, D. H. *Biotechnol. Prog.* **2003**, *19*, 1095.
(11) Cao, J.; Wang, Y.; Yu, J.; Xia, J.; Zhang, C.; Yin, D.; Häfeli, U. O. *J. Magn. Magn. Mater.* **2004**, *277*, 165.
(12) Park, S.; Kim, J. H.; Kim, C. O. *J. Magn. Magn. Mater.* **2004**, *272*, 2340.
(13) Yu, S.; Chow, G. M. *J. Mater. Chem.* **2004**, *14*, 2781.
(14) Levy, L.; Sahoo, Y.; Kim, K. S.; Bergey, E. J.; Prasad, P. N. *Chem. Mater.* **2002**, *14*, 3715.
(15) Berry, C. C.; Curtis, A. S. G. *J. Phys. D: Appl. Phys.* **2003**, *36*, R198.

10.1021/cm061861v CCC: $33.50
Published on Web 12/19/2006

tion, and polishing) scheme, which involves sequential, lengthy, and often costly unit operations. Functionalized magnetic particles could be tailored to selectively attach biomolecules of interest from a dilute bioliquor, coupled with the application of a magnetic field to separate them in a relatively nondestructive manner from other biological debris and fouling materials.[4] Hence, magnetic separation utilizing functionalized nanoparticles provides an excellent alternative for bioseparation. Despite the ongoing research efforts to discover synthesis routes that permit precise control of the properties of the magnetic particles through wet chemistry-based methods, such as microemulsion, sonochemical, reverse micelles, and sol−gel techniques, they are inherently limited in scalability. Some of the larger scale operations based on these techniques were only capable of producing around 10−15 g[8] and 20 g[16] of particles per batch. On the other hand, liquid-fed flame spray pyrolysis (FSP), which is a relatively recent hybrid of a flame aerosol technique, is a rapid, scalable, and waste-free process capable of producing up to 1.1 kg/h of nanoparticles on a pilot scale.[17] The versatility of FSP in producing simple,[18,19] composite[20−22] nanoparticles and even nanorods[23] with closely controlled characteristics has been extensively demonstrated in recent years. In fact, the recent advancement of FSP has enabled the synthesis of biomaterials such as the fluoroapatite and calcium phosphate bone replacement materials,[24] as well as transparent but radiopaque Ta_2O_5/SiO_2 for dental fillings.[25,26] The adaptation of FSP in synthesizing biocompatible nanomaterials therefore has great potentials.

In this work, we demonstrate the use of FSP for direct synthesis of superparamagnetic γ-Fe_2O_3 and SiO_2/γ-Fe_2O_3 nanoparticles with closely controlled particle size and morphology. In addition, coating of FSP-made bare γ-Fe_2O_3 with SiO_2 by conventional sol−gel technique was conducted as a comparison with the as-prepared FSP-synthesized SiO_2/γ-Fe_2O_3. Bovine serum albumin (BSA), as the most abundant protein found in bovine blood that shares a high percentage (76%) of sequence similarities with human serum albumin (HSA),[27] was used as the model protein for adsorption−desorption studies due to its simplicity, robustness, and the availability of vast literature on its adsorption behavior on metal oxide[28−30] and polymeric surfaces.[31]

2. Experimental Section

2.1. Materials. Iron(III) acetylacetonate ($Fe(acac)_3$, 97%), tetraethyl orthosilicate (TEOS, 98%), BSA (fraction V powder), Bradford reagent, acetonitrile, ammonium formate, formic acid, and ammonia solution (28%) were supplied by Sigma-Aldrich. Analytical grade xylene was obtained from Riedel-de-Haen. Ethanol, nitric acid, sodium hydroxide pellets, potassium dihydrogen orthophosphate, potassium hydrogen phosphate, and potassium chloride were purchased from Ajax Chemicals.

2.2. Particle Preparation. *2.2.1. Preparation of Magnetic Nanoparticles by FSP.* The Fe-only precursor for the synthesis of γ-Fe_2O_3 was prepared by dissolving 0.34 M $Fe(acac)_3$ in xylene/acetonitrile at a volume ratio of 63/22. This mixture had a combustion enthalpy of −26.7 kJ/mL. As for the SiO_2/γ-Fe_2O_3 synthesis, a predetermined amount of TEOS was added to obtain the desired Fe:Si ratio. The $Fe(acac)_3$ concentration was maintained at 0.34 M, while the xylene/acetonitrile ratio was adjusted to match the combustion enthalpy of Fe-only precursor. A flame spray pyrolysis reactor[32] was used to synthesize the particles in a single-step. The liquid precursor was delivered to the pressure-assisted nozzle (1.5 bar) using a syringe pump (Inotech R232), where it was atomized to produce fine droplets. For the synthesis of γ-Fe_2O_3, the ratios of liquid precursor feed flow rate (x mL/min) to dispersant O_2 gas flow rate (y L/min) were varied at 1:5, 10:5 and 12:3, while the synthesis of SiO_2/γ-Fe_2O_3 was only carried out at 10:5 ratio. The droplets were combusted by the surrounding methane/oxygen (1.5 L/min/3.2 L/min) supporting flame, forming a self-sustaining main core flame. An additional 5 L/min of sheath O_2 was provided through the outermost sintered metal ring. The product nanoparticles were collected on a glass fiber filter (Whatmann GF/D, 25.7 cm diameter) with the aid of a vacuum pump (Alcatel SD Series).

2.2.2. Particle Coating by Sol−Gel Technique. Silica coating of FSP γ-Fe_2O_3 particles was carried out according to a modified Stöber process.[33] Typically, 0.353 g of γ-Fe_2O_3 particles was suspended in a 492 mL mixture consisting of 439 mmol of NH_4-OH, 10.7 mol of Milli-Q water (Millipore), and 5.2 mol of ethanol. The suspension was sonicated for 40 min before 4.0 mmol of TEOS was added with stirring at 650 rpm. The mixture was left to react for 15 h, and the resulting coated particles were washed twice with ethanol and Milli-Q water sequentially before finally being left to dry in a 60 °C oven for 24 h. Each washing step consisted of particles recovery via centrifugation (Beckman Coulter Allegra 25R centrifuge) at 10 000 rpm for 15 min and redispersion ultrasonically.

2.3. Particle Characterization. Phase identification of the as-prepared powder was investigated using X-ray diffraction (XRD, Siemens D5000) utilizing Cu Kα radiation scanned for $2\theta = 20-70°$ with step size of 0.02° and scan speed of 0.6°/min. The crystallite sizes (d_{XRD}) of γ-Fe_2O_3 (311) phase were determined using the Scherrer formula. The size and morphology of the nanoparticles were observed using transmission electron microscopy (TEM, Phillips CM-200) at accelerating voltage of 200 kV, and

(16) Bruce, I. J.; Taylor, J.; Todd, M.; Davies, M. J.; Borioni, E.; Sangregorio, C.; Sen, T. *J. Magn. Magn. Mater.* **2004**, *284*, 145.
(17) Mueller, R.; Mädler, L.; Pratsinis, S. E. *Chem. Eng. Sci.* **2003**, *58*, 1969.
(18) Sokolowski, M.; Sokolowska, A.; Michalski, A.; Gokieli, B. *J. Aerosol Sci.* **1977**, *8*, 219.
(19) Mädler, L.; Stark, W. J.; Pratsinis, S. E. *J. Mater. Res.* **2002**, *17* (6), 1356.
(20) Strobel, R.; Stark, W. J.; Mädler, L.; Pratsinis, S. E.; Baiker, A. *J. Catal.* **2003**, *213*, 296.
(21) Stark, W. J.; Grunwaldt, J. D.; Maciejewski, M.; Pratsinis, S. E.; Baiker, A. *Chem. Mater.* **2005**, *17*, 3352.
(22) Strobel, R.; Mädler, L.; Piacentini, M.; Maciejewski, M.; Baiker, A.; Pratsinis, S. E. *Chem. Mater.* **2006**, *18*, 2532.
(23) Height, M.; Mädler, L.; Pratsinis, S. E.; Krumeich, F. *Chem. Mater.* **2006**, *18*, 572.
(24) Loher, S.; Stark, W. J.; Maciejewski, M.; Baiker, A.; Pratsinis, S. E.; Reichardt, D.; Maspero, F.; Krumeich, F.; Guenther, D. *Chem. Mater.* **2005**, *17*, 36.
(25) Schulz, H.; Mädler, L.; Pratsinis, S. E.; Burtscher, P.; Moszner, N. *Adv. Funct. Mater.* **2005**, *15*, 830.
(26) Mädler, L.; Krumeich, F.; Burtscher, P.; Moszner, N. *J. Nanopart. Res.* **2006**, *8*, 323.
(27) Rezwan, K.; Meier, L. P.; Rezwan, M.; Vörös, J.; Textor, M.; Gauckler, L. J. *Langmuir* **2004**, *20*, 10055.
(28) Fukuzaki, S.; Urano, H.; Nagata, K. *J. Ferment. Bioeng.* **1996**, *81*, 163.
(29) Larsericsdotter, H.; Oscarsson, S.; Bujis. J. *J. Colloid Interface Sci.* **2005**, *289* (1), 26.
(30) Rezwan, K.; Meier, L. P.; Gauckler, L. J. *Biomaterials* **2005**, *26*, 4351.
(31) Yoon, J. Y.; Park, H. Y.; Kim, J. H.; Kim, W. S. *J. Colloid Interface Sci.* **1996**, *177*, 613.
(32) Mädler, L.; Kammler, H. K.; Mueller, R.; Pratsinis, S. E. *J. Aerosol Sci.* **2002**, *33*, 369.
(33) Stöber, W.; Fink, A.; Bihn, E. *J. Colloid Interface Sci.* **1968**, *26*, 62.

the γ-Fe_2O_3 size distribution was determined on the basis of at least 150 sample counts. The specific surface area (SSA) of the particles was measured by means of nitrogen adsorption at 77 K (Micromeritics Tristar 3000) following the Brunauer−Emmett−Teller (BET) method. The magnetic properties were measured using a Quantum Design 7 T MPMS SQUID magnetometer between 5 and 400 K. Acid dissolution studies were performed by suspending 500 mg/L particles in 1 M nitric acid for 5 h and filtered using a cellulose membrane (0.2 μm, Sartorius). The filtrate Fe concentration was measured using an induced coupled plasma-atomic emission spectrometer (ICP-AES, Varian). Chemical composition analysis was carried out by fully digesting the particles in aqua regia and hydrofluoric acid. The aliquot was analyzed for Si and Fe elemental concentrations on an induced coupled plasma-optical emission spectrometer (ICP-OES, GBC Integra XMP). The particle ζ potential was measured by means of electrophoretic mobility using the Brookhaven ZetaPlus analyzer at 250 mg/L particle concentration.

2.4. Protein Adsorption and Desorption. Magnetic particles (2.5 g L^{-1}) were suspended in a series of phosphate and formate (10 mM, pH 5.3) buffers with initial BSA concentration ranging from 0.1 to 1.6 g L^{-1}. The suspensions were placed on a roller (Ratek) at room temperature for 3 h to reach adsorption equilibrium. Preliminary experiments showed that 3 h were sufficient to reach equilibrium. After batch settling of the mixture on a neodymium magnet (AMF Magnetics, Australia), the supernatant containing BSA was separated from the particles held by the magnet at the bottom of the adsorption vials. The supernatant BSA concentrations were determined following the Bradford method[34] using a UV-visible spectrophotometer (Varian Cary 300 Scan). The amount of BSA adsorbed was calculated by mass balance. The data was fitted to the Langmuir adsorption isotherm.

BSA desorption was performed following the adsorption onto γ-Fe_2O_3 and SiO_2/γ-Fe_2O_3 particles at an initial BSA concentration of 1.0 g L^{-1} in phosphate and formate buffers (10 mM, pH 5.3). After adsorption, particles were recovered magnetically and various desorbing agents—KH_2PO_4 (pH 9.6), KOH (pH 9.6), 1 M KCl dissolved in 10 mM formate buffer (pH 5.3), and 1 M KCl dissolved in 10 mM phosphate buffer (pH 5.3), respectively—were subsequently introduced. The samples were placed on a roller for a further 2 h, after which the particles were separated by magnetic settling and the supernatant analyzed for BSA concentration.

After adsorption−desorption studies, the particles in formate and phosphate buffers were magnetically recovered and vacuum-dried at room temperature. The particle surfaces were examined with attenuated total reflectance Fourier-transform infrared spectrometer (ATR-FTIR, Bruker). A total of 30 spectral scans were repeated over the range of 650−4000 cm^{-1} with a 2 cm^{-1} resolution.

3. Results and Discussion

3.1. Particle Characterization. *3.1.1. Crystallography, Morphology, and Size of Bare γ-Fe_2O_3.* Flame spray pyrolysis of iron(III) acetylacetonate in xylene/acetonitrile resulted in the formation of dark brownish iron oxide particles. The X-ray diffraction (XRD) pattern (Figures 1a−c) of the particles was matched closely to crystalline maghemite (γ-Fe_2O_3, PDF: 004-0755), although the presence of the magnetite (Fe_3O_4, PDF: 019-0629) phase could not be entirely ruled out due to the similarity in Bragg peaks. Increasing the ratio of liquid precursor feed flow rate (mL/min) to dispersion O_2 (L/min) from 1:5 to 10:5 to 12:3 during synthesis resulted in the sharpening of diffraction peaks. The crystallite sizes were obtained by correlating with Scherrer formula at the γ-Fe_2O_3 (311) peak to give d_{XRD} of 6, 14, and 21 nm, respectively. For γ-Fe_2O_3 sample with d_{XRD} = 6 nm, an amorphous-like peak broadening and overlapping between (220) and (311) peaks was evident due to its small crystallite size (Figure 1a). It is well-established that increasing the liquid precursor feed flow rate to dispersion gas ratio increases the metal concentration, rate of combustion enthalpy released, and longer residence time of the flame. This gives rise to the increased coalescence and sintering within the flame and hence the formation of larger particles as reported in the FSP synthesis of many simple metal oxide systems. The increase in γ-Fe_2O_3 particle diameter with gaseous iron pentacarbonyl $Fe(CO)_5$ precursor concentration in a low-pressure H_2/O_2/Ar flame was previously reported by Janzen et al.[35]

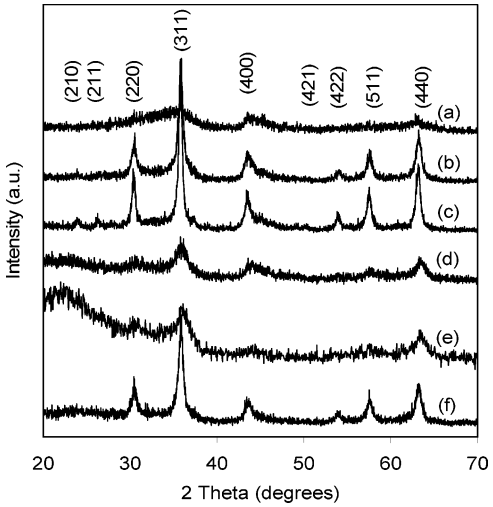

Figure 1. X-ray diffraction patterns of FSP γ-Fe_2O_3 with d_{XRD} of (a) 6, (b) 14, and (c) 21 nm; FSP SiO_2/γ-Fe_2O_3 with Fe:Si of (d) 1:2 and (e) 1:5; and (f) sol−gel-coated SiO_2/γ-Fe_2O_3 (Fe:Si = 1:1, ICP).

The FSP-synthesized γ-Fe_2O_3 particles showed a uniform hexagonal shape as observed under transmission electron microscopy (TEM) (Figure 2). Clear lattice fringes in Figure 2c further indicated the existence of well-defined single-crystalline particles. Image analysis of the particles at tilted angles (−30° and +30°) with in situ TEM showed the occurrence of platelet-shaped particles as shown by the relatively uniform contrast within each particle, as well as the absence of corner effects and shape variation when tilted typical for 2-D structure. Further investigation by atomic force microscopy (AFM) was found to agree well with the TEM observation that the particles were indeed platelets. Interestingly, the geometric mean diameter of the γ-Fe_2O_3 particles observed visually from TEM images (d_{TEM}) agreed well with d_{XRD} at the γ-Fe_2O_3 (311) phase. For bare γ-Fe_2O_3, the particle size distribution could be described by a log-normal distribution with a geometric standard deviation of 1.4−1.5 (Figure 2) which is close to the theoretical self-preserving size distribution (SPSD) of 1.46.[36]

Analysis of the particle specific surface area (SSA) by N_2 adsorption showed a consistently lower BET-equivalent

(34) Bradford, M. M. *Anal. Biochem.* **1976**, *72*, 248.

(35) Janzen, C.; Roth, P. *Combust. Flame* **2001**, *125*, 1150.

(36) Pratsinis, S. E. *Prog. Energy Combust. Sci.* **1998**, *24*, 197.

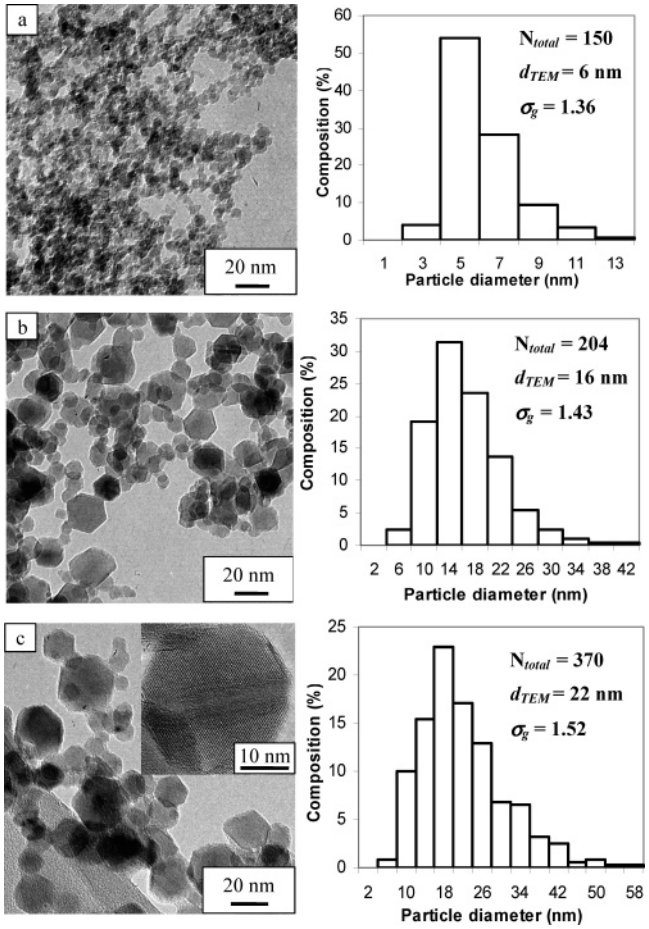

Figure 2. TEM micrographs of FSP γ-Fe_2O_3 with d_{XRD} of (a) 6, (b) 14, and (c) 21 nm and the corresponding particle size distribution.

diameter (d_{BET}) compared with d_{TEM} (Table 1), in further agreement with the hexagonal platelet-shaped γ-Fe_2O_3 particles observed under TEM. The platelet-shaped morphology of FSP-synthesized γ-Fe_2O_3 provided a high surface area to volume ratio compared to spherical-shaped particles, rendering them a better choice as adsorbent. All of the γ-Fe_2O_3 samples prepared in this work exhibited the type IV N_2 adsorption−desorption isotherm with weak hysteresis (Table 1) arising from the voids between nonporous particles. This is a unique characteristic of particles synthesized via the gas-to-particle route, where nanoparticles are formed by condensation of metal vapor during in situ supersaturation of the flame.[36] Porous magnetic particles were previously reported to be susceptible to entrapment and fouling by biomolecules within the pores, posing difficulties in cleaning and regeneration of adsorbents during bioseparation. Thus high surface areas combined with nonporous structures of the FSP-made nanoparticles are potentially beneficial aspects for their uses in bioapplications.

3.1.2. Crystallography, Morphology, and Size of SiO_2/γ-Fe_2O_3. Incorporation of tetraethyl orthosilicate (TEOS) in the liquid precursor at Fe:Si ratios of 1:2 and 1:5 did not result in the formation of silicates, despite the high temperature of the flame. In fact, XRD spectra (Figure 1d,e) of the as-prepared particles displayed similar Bragg peaks as that of bare γ-Fe_2O_3, hence also ruling out the possibility of forming solid solution. An amorphous SiO_2 hump ($2\theta = 20-40°$) could be observed for both FSP-made SiO_2/γ-Fe_2O_3 and was more distinctive at higher SiO_2 content. Elemental analysis of dissolved FSP-made particles by ICP-OES confirmed an almost equal Fe and Si composition as the ratio used in the liquid precursors (Table 1). Despite the same combustion enthalpy (−26.7 kJ/mL), precursor feed flow rate (mL/min) to dispersion O_2 (L/min) ratio (10:5), and Fe concentration carried out during the FSP synthesis of SiO_2/γ-Fe_2O_3 at Fe:Si ratio of 1:2 and 1:5, a significant difference in terms of γ-Fe_2O_3 crystallite sizes was detected between the two. The d_{XRD} of γ-Fe_2O_3 decreased from 8 nm for Fe:Si = 1:2 to 4 nm for Fe:Si = 1:5.

TEM images of the SiO_2/γ-Fe_2O_3 nanocomposite displayed a distinct but different segregation between SiO_2 and γ-Fe_2O_3 phases made at Fe:Si of 1:2 (Figure 3a,b) and 1:5 (Figure 3c,d). At Fe:Si ratio of the 1:2, γ-Fe_2O_3 phase was visibly segregated to the edge of every silica particle. On the other hand, well-dispersed multicores γ-Fe_2O_3 embedded in spherical silica particles were observed at a Fe:Si ratio of 1:5. Unlike the bare γ-Fe_2O_3 particles, the γ-Fe_2O_3 cores did not assume the hexagonal platelet structure in the presence of SiO_2, suggesting that platelet structure was only formed in the later stage in the flame and SiO_2 suppressed this morphological transformation. Similar composite conformations were also reported by Ehrman et al.[37] from the combustion of hexamethyl disiloxane and $Fe(CO)_5$ in a vapor-fed premixed methane flame reactor. The composite conformations in this work and that of Ehrman et al.[37] appeared to be governed by the thermodynamics of Fe−Si phase at high temperature, as reported by the latter. They further observed an almost complete segregation in the composite particles where the presence of Fe atoms in Si-rich phase was undetectable. The visually determined d_{TEM} for γ-Fe_2O_3 cores in both Fe:Si of 1:2 and 1:5 (Figures 3a−d) were significantly larger than the Scherrer-derived d_{XRD} (Table 1), possibly due to a different plane other than (311) observed under TEM. The γ-Fe_2O_3 core size distribution (σ_g = 1.39) for Fe:Si of 1:2 was close to that of self-preserving

Table 1. Summary of Physical and Chemical Properties of γ-Fe_2O_3 and SiO_2/γ-Fe_2O_3 Nanoparticles

	FSP synthesis		composition		N_2 adsorption			XRD	particle counting		dissolution
	precursor feed (mL/min)	dispersion O_2 (L/min)	Fe:Si ratio nominal	ICP	isotherm type	SSA (m^2/g)	d_{BET} (nm)	d_{XRD} (nm)	d_{TEM} (γ-Fe_2O_3) (nm)	σ_g	[Fe] (ppm)
FSP γ-Fe_2O_3	1	5	−	−	IV	229	5	6	6	1.36	−
	10	5	−	−	IV	94	13	14	16	1.43	25
	12	3	−	−	IV	61	20	21	22	1.52	−
FSP SiO_2/γ-Fe_2O_3	10	5	1:2	1:1.8	IV	99	17	8	19	1.39	5
	10	5	1:5	1:4.5	IV	80	24	4	11	1.27	4
sol-gel SiO_2/γ-Fe_2O_3	−	−	1:1	1:0.7	IV	120	14	13	17	1.41	1

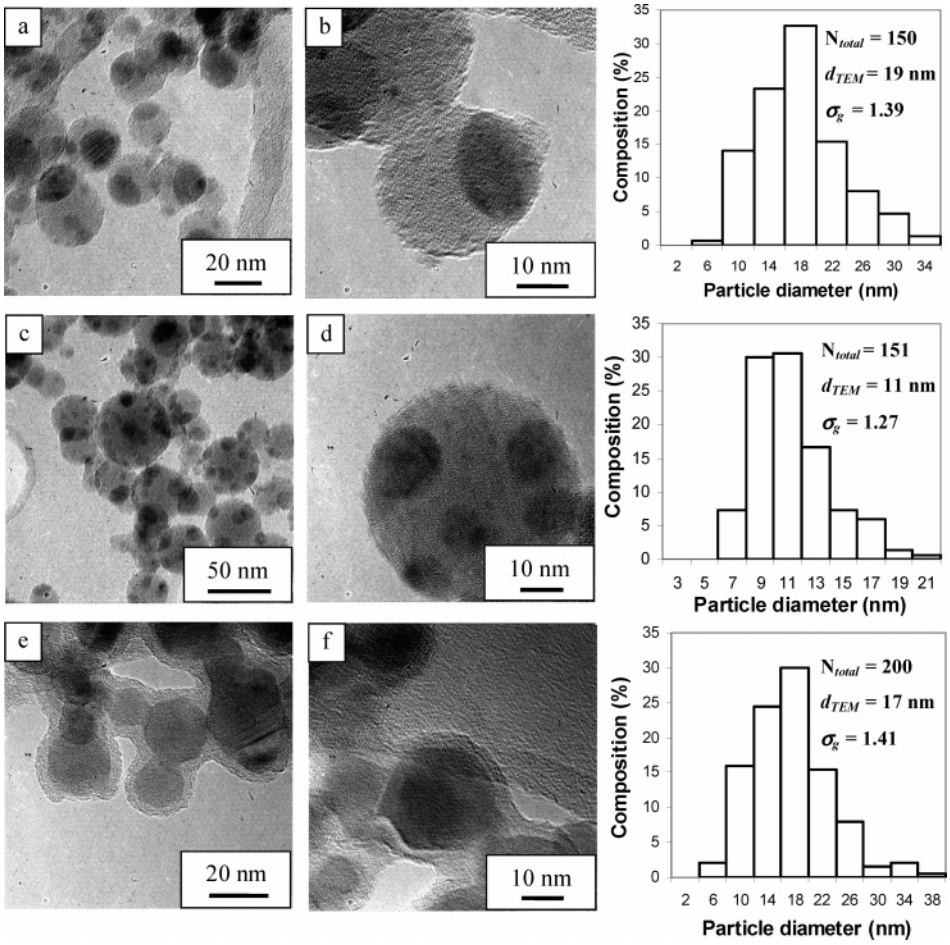

Figure 3. TEM micrographs of FSP SiO_2/γ-Fe_2O_3 with Fe:Si of (a, b) 1:2 and (c, d) 1:5 and (e, f) sol−gel-coated SiO_2/γ-Fe_2O_3. Also shown are the corresponding γ-Fe_2O_3 core size distribution.

size distribution. However, the suppression of γ-Fe_2O_3 coagulation within the SiO_2 matrix in Fe:Si of 1:5 resulted in a narrower size distribution (σ_g = 1.27) than SPSD, in addition to the morphological transformation as mentioned earlier. Perhaps also important to reiterate is the fact that both SiO_2/γ-Fe_2O_3 composites (Fe:Si = 1:2 and 1:5) were sprayed at the same rate of combustion enthalpy and Fe concentration; hence, the difference in size distributions could not be attributed to these two factors. Ehrman et al. suggested that coagulation of γ-Fe_2O_3 in SiO_2 was driven by liquid or solid-state diffusion.[37] As the FSP-made SiO_2/γ-Fe_2O_3 particles were nonporous and spherical with weak hysteresis in type IV isotherm arising from voids between particles, d_{BET} provides an excellent quantitative analysis on the overall particle size (Table 1).

As a comparison to FSP-made SiO_2/γ-Fe_2O_3, the as-prepared γ-Fe_2O_3 (d_{XRD} = 14 nm) was coated with SiO_2 using a modified Stöber sol−gel technique.[33] This technique produced a uniform, thin (∼1−2 nm), and amorphous silica coating around the γ-Fe_2O_3 core (Figure 3e, f). The coating method did not achieve individual core−shell structures but rather a continuous silica layer around a few γ-Fe_2O_3 particles. Woo et al.[38] also reported that silica−magnetite nanoparticles formed by TEOS hydrolysis were connected by interparticle gelation during silica coating. The sol−gel coating process involves the formation of silica through TEOS hydrolysis that replaces the alkyloxide groups with hydroxyl groups, followed by a condensation reaction producing siloxane bonds Si−O−Si from silanol groups. The kinetics of the sol−gel silica coating process depends on the type of alcohol, alcohol to water ratio, ammonia concentration, the amount of TEOS, and temperature.[39,40] Deng et al.[39] reported that silica-coated magnetite can be formed from an ethanol to water volume ratio of 2−4, with a higher water content increasing the speed of hydrolysis. At ethanol to water ratio of less than 2, the nanoparticles showed irregular morphology or even no coating at all. The modified Stöber process used in this work utilized relatively high water content (ethanol to water ratio of 1.5) but still maintained the composite structures with thin coating. The coating yielded SiO_2/γ-Fe_2O_3 with a Fe:Si ratio of 1:0.7, as determined from digestion of coated particles (Table 1).

The crystalline γ-Fe_2O_3 core of the sol−gel-coated particle was unaffected by the modified room-temperature Stöber technique, as evident from the XRD analysis (Figure 1f). In addition, the d_{XRD} of γ-Fe_2O_3 core before (14 nm) and after

(37) Ehrman, S. H.; Friedlander, S. K. *J. Mater. Res.* **1999**, *14* (12), 4551.
(38) Woo, K.; Hong, J.; Ahn, J-P. *J. Magn. Magn. Mater.* **2005**, *293*, 177.
(39) Deng, Y. H.; Wang, C. C.; Hu, J. H.; Yang, W. L.; Fu, S. K. *Colloids Surf. A* **2005**, *262*, 87.
(40) Rao, K. S.; El-Hami, K.; Kodaki, T.; Matsushige, K.; Makino, K. *J. Colloid Interface Sci.* **2005**, *289*, 125.

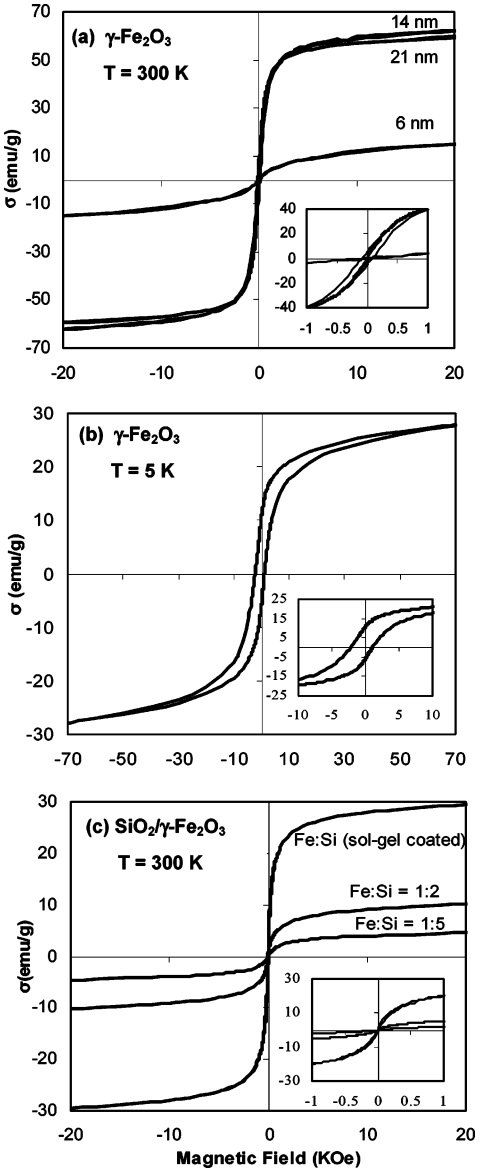

Figure 4. Hysteresis loops of (a) FSP γ-Fe_2O_3 at 300 K, (b) 6 nm FSP γ-Fe_2O_3 at 5 K, and (c) SiO_2/γ-Fe_2O_3 at 300 K.

sol−gel coating (13 nm) was almost identical (Table 1). A SiO_2 peak was absent from the XRD spectrum of the sol−gel-coated SiO_2/γ-Fe_2O_3, presumably due to the low SiO_2 concentration and thin coating. The SiO_2 coating was nonporous as shown by the indifferent N_2 adsorption−desorption isotherm observed for FSP particles, despite the porous structure often obtained from sol−gel preparation.[41] The surface morphology of SiO_2 coating seemed to be dependent on the morphology of the γ-Fe_2O_3 core. The difference between d_{BET} and d_{XRD} of the sol−gel-coated SiO_2/γ-Fe_2O_3 (Table 1) was only 1 nm, in qualitative agreement with the observed thickness under TEM.

3.1.3. Magnetic Properties. The hysteresis loops at 300 K (Figure 4a) indicated that all three FSP γ-Fe_2O_3 samples (d_{XRD} = 6, 14, and 21 nm) were predominantly superparamagnetic at room temperature, with the 6-nm sample having essentially no blocked (ferromagnetic) particles while the 14 and 21 nm samples had a progressively greater amount of blocked particles (Figure 4a, inset). Hysteresis loops were also collected at 5 K following field cooling in a 7 T field from room temperature. These loops were used to determine the specific saturation magnetization (σ_s) and coercivity (H_c) of the samples, as well as the presence of exchange bias in the samples at 5 K (Table 2). Exchange bias is when the center of a hysteresis loop is shifted along the field axis due to coupling between ferromagnetic and antiferromagnetic spins.[42] An example of a 5 K hysteresis loop is shown for a 6-nm sample in Figure 4b, which shows a shifting of a loop along the field axis due to exchange bias.

Table 2. Summary of Magnetic Properties of γ-Fe_2O_3 and SiO_2/γ-Fe_2O_3 Nanoparticles

		σ_s (emu/g)[a]	H_c (Oe)	H_e (Oe)	d_{SQUID} (nm)
FSP γ-Fe_2O_3	d_{XRD} = 6 nm	20.8	1610	610	4
	d_{XRD} = 14 nm	73.6	460	45	8
	d_{XRD} = 21 nm	68.8	425	25	11
FSP SiO_2/γ-Fe_2O_3	Fe:Si = 1:2	38.2	760	235	9
	Fe:Si = 1:5	40.0	825	275	8
SiO_2/γ-Fe_2O_3	sol-gel coated	53.4	512	63	11

[a] σ_s was calculated per unit mass of γ-Fe_2O_3 in the SiO_2/γ-Fe_2O_3 composite materials assuming all Fe in the form of γ-Fe_2O_3.

The specific saturation magnetization of the d_{XRD} = 14 and 21 nm samples was similar with magnitude only slightly less than the bulk values for γ-Fe_2O_3 of approximately 74 emu/g.[43] However, the specific saturation magnetization of the 6-nm sample (20.8 emu/g) was significantly lower than the theoretical value. Variable and often low magnetization values for γ-Fe_2O_3 nanoparticles have been observed by a number of authors.[44−45] Low magnetization values have been associated with high coercivity and the presence of exchange bias at low temperature, which was observed here for the 6-nm sample. This effect of decreased magnetization for small particle size was originally thought to be a surface effect, but a recent work has shown that low magnetization values and associated changes to the hysteresis loops were predominately a result of a disordered structure.[46] The small crystallite sizes of 6-nm γ-Fe_2O_3 sample (Figure 1a) with amorphous-like XRD spectrum indicated some extent of the aforementioned disordered nature.

An estimate of particle size, d_{SQUID}, was obtained by fitting the magnetization curves at 390 K with a Langevin function numerically integrated over a distribution of particles sizes[47] (Table 2). In order to fit the data, a form of particle distribution must be assumed;[48] in this case, a log-normal distribution was chosen as demonstrated earlier for the size distribution from TEM particle counting. It should be noted that particles that were blocked at the measurement temper-

(41) Liu, Q.; Xu, Z; Finch, J. A.; Egerton, R. *Chem. Mater.* **1998**, *10*, 3936.
(42) Stamps, R. L. *J. Phys. D: Appl. Phys.* **2000**, *33*, R247.
(43) Berkowitz, A. E.; Schuele, W. J.; Flanders, P. J. *J. Appl. Phys.* **1968**, *39 (2)*, 1261.
(44) Morales, M. P.; Veintemillas-Verdaguer, S.; Montero, M. I.; Serna, C. J.; Roig, A.; Casas, L.; Martînez, B.; Sandiumenge, F. *Chem. Mater.* **1999**, *11*, 3058.
(45) Fiorani, D.; Testa, A. M.; Lucari, F.; D'Orazio, F.; Romero, H. *Phys. B* **2002**, *320*, 122.
(46) Serna, C. J.; Bødker, F.; Mørup, S.; Morales, M. P.; Sandiumenge, F.; Veintemillas-Verdaguer, S. *Solid State Commun.* **2001**, *118*, 437.
(47) Chantrell, R. W.; Popplewell, J.; Charles, S. W. *IEEE Trans. Magn.* **1978**, *14*, 975.
(48) Berkov, D. V.; Görnert, P.; Buske, N.; Gansau, C.; Muller, J.; Giersig, M.; Neumann, W.; Su, D. *J. Phys. D: Appl. Phys.* **2000**, *33*, 331.

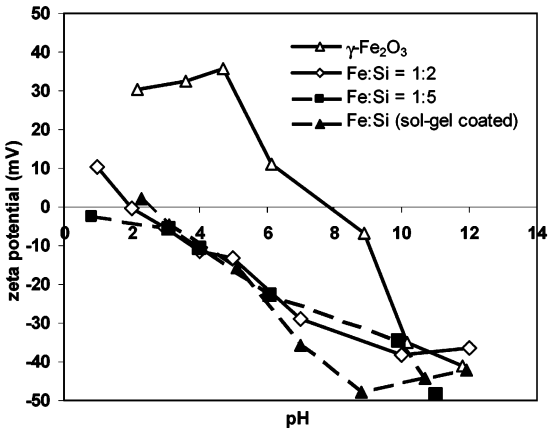

Figure 5. ζ-Potential profile of γ-Fe_2O_3 and SiO_2/γ-Fe_2O_3 at different pH (250 mg/L particle loading, 50 mM KNO_3 background electrolyte).

ature would cause errors in the measured particle size distribution. As such, the measured size was simply an indication of the relative volume-based diameter of superparamagnetic material in the samples. The diameter determined from fitting the magnetization curves, d_{SQUID}, was much smaller than that of d_{XRD}, d_{TEM}, and d_{BET} for all γ-Fe_2O_3 particles. This is not surprising given the 2-D shape of the particles, as confirmed by TEM tilting experiments and AFM, and the assumptions made by each technique when calculating the diameter. For example, BET assumes spherical particles and calculates particle size based on the measured surface area, while the magnetic measurements also assumes spherical particles but calculates diameters based on particle volume; both of these numbers will be smaller than the platelet diameters measured by TEM.

Hysteresis loops for the SiO_2/γ-Fe_2O_3 composite materials at 300 K are shown in Figure 4c. The magnetization of these samples was lower than the FSP γ-Fe_2O_3 samples due to the presence of SiO_2, as well as the decrease in magnetic core size (Table 1), in agreement with SiO_2/γ-Fe_2O_3 particles prepared by other techniques, such as chemical vapor condensation.[49] The chemical compositions of Fe and Si as determined by ICP-OES (Table 1) was used to calculate the specific saturation magnetization of the γ-Fe_2O_3 cores in each of the samples at 5 K (Table 2). These results showed that the specific magnetization per unit mass of γ-Fe_2O_3 cores was significantly lower than both the bulk values and the measured values for FSP γ-Fe_2O_3 of d_{XRD} 14 and 21 nm. This could be either due to the disordered γ-Fe_2O_3 or the presence of alternate phases of Fe oxides. This also explains the discrepancies between d_{TEM} (11−19 nm) in comparison to d_{SQUID} (8−9 nm) and d_{XRD} (4−8 nm) of γ-Fe_2O_3 in SiO_2/γ-Fe_2O_3 particles.

3.1.4. Isoelectric Point and Acid Dissolution Studies. The isoelectric point (IEP) of the FSP-made γ-Fe_2O_3 particles was determined to be ∼pH 8 (Figure 5), in agreement with coprecipitated maghemite particles.[13] On the other hand, the IEP of SiO_2/γ-Fe_2O_3 particles (FSP-made and sol−gel-coated) were shifted to pH 1−2, corresponding to the IEP of SiO_2. The result indicated the presence of mostly SiO_2 on the particle surface, even though a complete encapsulation of γ-Fe_2O_3 cores by SiO_2 could not be completely ascertained. However, the similarity in ζ-potential curve of FSP-made and sol−gel-coated SiO_2/γ-Fe_2O_3 particles did suggest a similarity in surface electrostatic properties of these particles, despite differences in morphology. Surface FT−IR spectra reported by Ehrman et al.[37] on flame-made SiO_2/γ-Fe_2O_3 particles found a mixture of a weak band (610 cm^{-1}) originating from γ-Fe_2O_3 and Si−O−Si bands (800 and 1100 cm^{-1}) for particles with Fe:Si of 1:1, implying surface exposure of γ-Fe_2O_3. As for the particles with Fe:Si of 1:5, only the Si−O−Si bands could be observed, indicating minimal surface exposed γ-Fe_2O_3 in the latter. On the basis of their results, it was envisaged that some extent of γ-Fe_2O_3 surface exposure still existed for Fe:Si of 1:2 in the current work, given its similarity in particle morphology to that of 1:1 Fe:Si in Ehrman et al.[37]

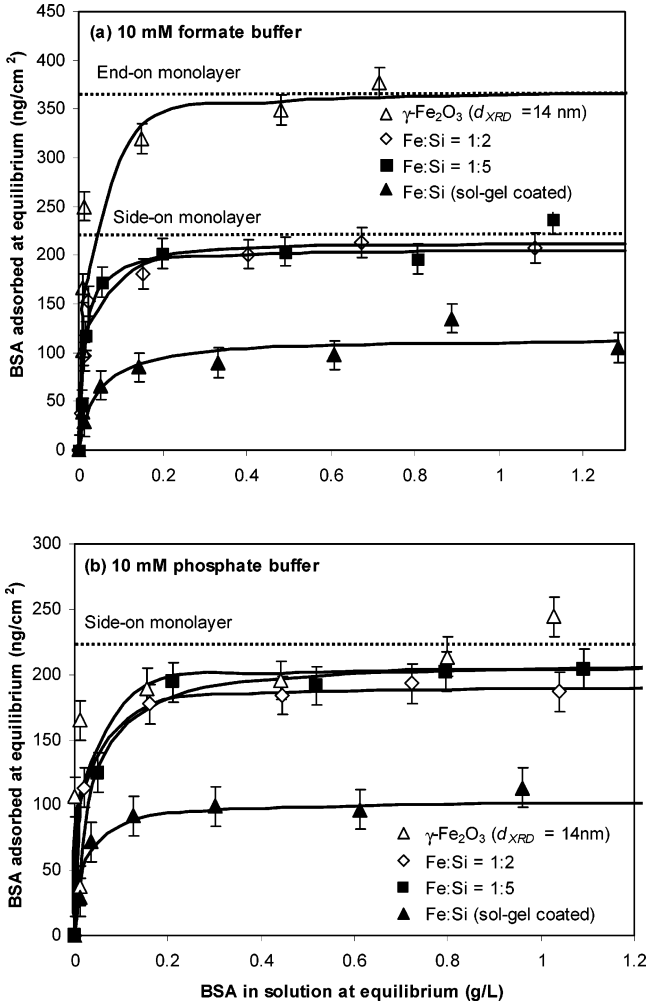

Figure 6. BSA adsorption isotherms of γ-Fe_2O_3 and SiO_2/γ-Fe_2O_3 in (a) 10 mM formate buffer and (b) 10 mM phosphate buffer (2.5 g/L particle loading, pH 5.3).

Further investigation was carried out through acid dissolution studies on all SiO_2/γ-Fe_2O_3 particles in 1 M nitric acid. Table 1 shows the different extent of Fe leaching into the suspension over a 5 h period, in the order of sol−gel < Fe:Si 1:5 < Fe:Si 1:2 ≪ bare γ-Fe_2O_3. The result implied an almost complete encapsulation of γ-Fe_2O_3 cores by the SiO_2 layer during sol−gel coating, in agreement with the

(49) Yu, J. H.; Lee, C. W.; Im, S. S.; Lee, J. S. *Rev. Adv. Mater. Sci.* **2003**, *4*, 55.

Table 3. ζ-Potential of Fresh γ-Fe_2O_3 and SiO_2/γ-Fe_2O_3, after BSA Adsorption and after Desorption

		10 mM formate buffer					10 mM phosphate buffer				
				ζ (mV)					ζ (mV)		
		Q_{max} (mg/g)	$K_d \times 10^{-2}$ (g/L)	before adsorption	after adsorption	after desorption (KOH)	Q_{max} (mg/g)	$K_d \times 10^{-2}$ (g/L)	before adsorption	after adsorption	after desorption (K_2HPO_4)
γ-Fe_2O_3	$d_{XRD} = 14$ nm	348	1.59	26	−9	−36	194	1.12	−40	−12	−27
FSP SiO_2/γ-Fe_2O_3	Fe:Si = 1:2	205	1.36	−35	−25	−36	190	1.40	−35	−10	−26
	Fe:Si = 1:5	172	1.47	−33	−23	−38	169	3.23	−32	−9	−20
SiO_2/γ-Fe_2O_3	sol-gel coated	138	4.37	−28	−24	−39	124	2.07	−24	−6	−27

observation from TEM images. On the other hand, phase segregation in FSP-made SiO_2/γ-Fe_2O_3 particles led to a minor exposure of γ-Fe_2O_3 on the particle surface. However, the amount of exposed γ-Fe_2O_3 was probably too little to cause significant effect on the particle ζ-potential measurement.

3.2. BSA Adsorption and Desorption. *3.2.1. Adsorption Isotherms and Conformation Studies.* The BSA monomer structure is heart-shaped, with dimensions of $9 \times 5.5 \times 5.5$ nm^3 and an IEP of around 4.7−5.[27] In this work, the adsorption trends of BSA onto γ-Fe_2O_3 and SiO_2/γ-Fe_2O_3 particles in formate (Figure 6a) and phosphate (Figure 6b) buffers were found to obey Langmuir isotherm, as observed for a range of adsorbents such as silica, titania, zirconia, and alumina.[28] The saturation adsorption value of BSA onto the hydrophobic γ-Fe_2O_3[15] particles ($d_{XRD} = 14$ nm) in formate buffer correlated well with a reported value of 365 ng/cm^2 for an end-on (5.5×5.5 nm^2) BSA monolayer adsorption.[27] On the other hand, the maximum BSA adsorption capacity was in agreement with the value (223 ng/cm^2) reported for a side-on (9×5.5 nm^2)[27] BSA monolayer for the same particle in phosphate buffer and for all FSP-synthesized SiO_2/γ-Fe_2O_3 particles in both buffers. Formation of BSA dimer previously observed for Al_2O_3 particles[27] is ruled out in this study, as the adsorption was in strict conformation with the Langmuir adsorption isotherm. Moreover, formation of dimer on top of the adsorbed monolayer, which would have resulted in a maximum value of twice the Langmuir saturation adsorption capacity, was not observed in the present work either. The small dissociation constant (K_d) values of BSA on γ-Fe_2O_3 particles calculated to be 0.016 and 0.011 g/L in formate and phosphate buffers, respectively, show a high affinity of BSA to the particle surfaces (Table 3).

To further investigate the orientation of BSA adsorbed on the magnetic particles, we have calculated the net charges for the three domains of BSA at the working pH of 5.3. The charges of these domains were calculated to be −4.1, 0.4, and 3.6, respectively, for domains I, II and III based on the 582 amino acid sequence of BSA reported by Peters.[50] The unequal charge distribution was due to the different numbers of charged amino acids constituting each domain. The asymmetry of local charge distribution in BSA across the three domains should allow BSA to adsorb onto charged particle surface in its preferred orientation, driven by the particle−BSA electrostatic interaction. For example, γ-Fe_2O_3 particles in formate buffer were positively charged ($\zeta = +26$ mV, Table 3), and BSA adsorption on γ-Fe_2O_3 surface was earlier shown to take place by end-on monolayer conformation (Figure 6a). Hence, the preferred orientation of BSA adsorbing onto the positively charged particle surface would be through the most negatively charged domain I, leaving the two positively charged domains II and III protruding into the solution (Figure 7). Adsorption of BSA on γ-Fe_2O_3 particles surface was also verified by FT−IR analysis as shown by the additional BSA characteristic peaks at 3284, 1640, and 1516 cm^{-1} (Figure 8a, ii), corresponding to N−H stretching and amide I and II, respectively.[51,52]

The saturation adsorption capacity of BSA onto FSP-made SiO_2/γ-Fe_2O_3 particles in formate buffer corresponded closely to side-on monolayer coverage (Figure 6a), with negative ζ-potential, even before BSA adsorption (Table 3). Thus the adsorption of BSA monomer onto the negatively charged SiO_2/γ-Fe_2O_3 particles was most likely to have occurred from the sides having positively charged domains II and III, leaving the negatively charged domain I exposed. This was confirmed by the highly negatively charged ζ-potential after adsorption ($\zeta = -24$ mV, Table 3).

The saturation adsorption capacities of BSA onto FSP-made γ-Fe_2O_3 and SiO_2/γ-Fe_2O_3 particles were similar in phosphate buffer (Figure 6b) with both corresponded closely to side-on BSA monolayer coverage. Interestingly, ζ-potential measurements also revealed that both particles had similar ζ-potential values after BSA adsorption (Table 3). The low ζ-potential values, ranging from −9 to −12 mV, implied that BSA adsorption would likely to have occurred along domains I and II, rendering the positively charged domain III protruding in the solution (Figure 7). As domains I and II were not entirely shielded by domain III due to the geometry of BSA (Figure 7a), it would neutralize to some extent an otherwise positively charged surface, thereby causing the surface to be slightly negative instead. It is worth to note that BSA adsorbed with different orientations on SiO_2/γ-Fe_2O_3 particles in formate and phosphate buffers despite the similar adsorption capacity and side-on conformation. The presence of phosphate ions, irrespective of the particles surface (γ-Fe_2O_3 and SiO_2/γ-Fe_2O_3), was thought to interact well with domains I and II (which are rich in aspartic acid and glutamic acids), causing the BSA molecule to orientate with its most negatively charged sides approaching the surface. The specific adsorption of phosphate anions ($H_2PO_4^-$ and HPO_4^{2-}) onto γ-Fe_2O_3 particle surface was indicated by the strongly negative ζ-potential (−40 mV) of

(50) Peters, T. JR. *Adv. Protein Chem.* **1985**, *37*, 161.
(51) Mikhaylova, M.; Kim, D. K.; Berry, C. C.; Zagorodni, A.; Toprak, M.; Curtis, A. S. G.; Muhammed, M. *Chem. Mater.* **2004**, *16*, 2344.
(52) Oldani, M.; Schock, G. *J. Membr. Sci.* **1989**, *43*, 243.

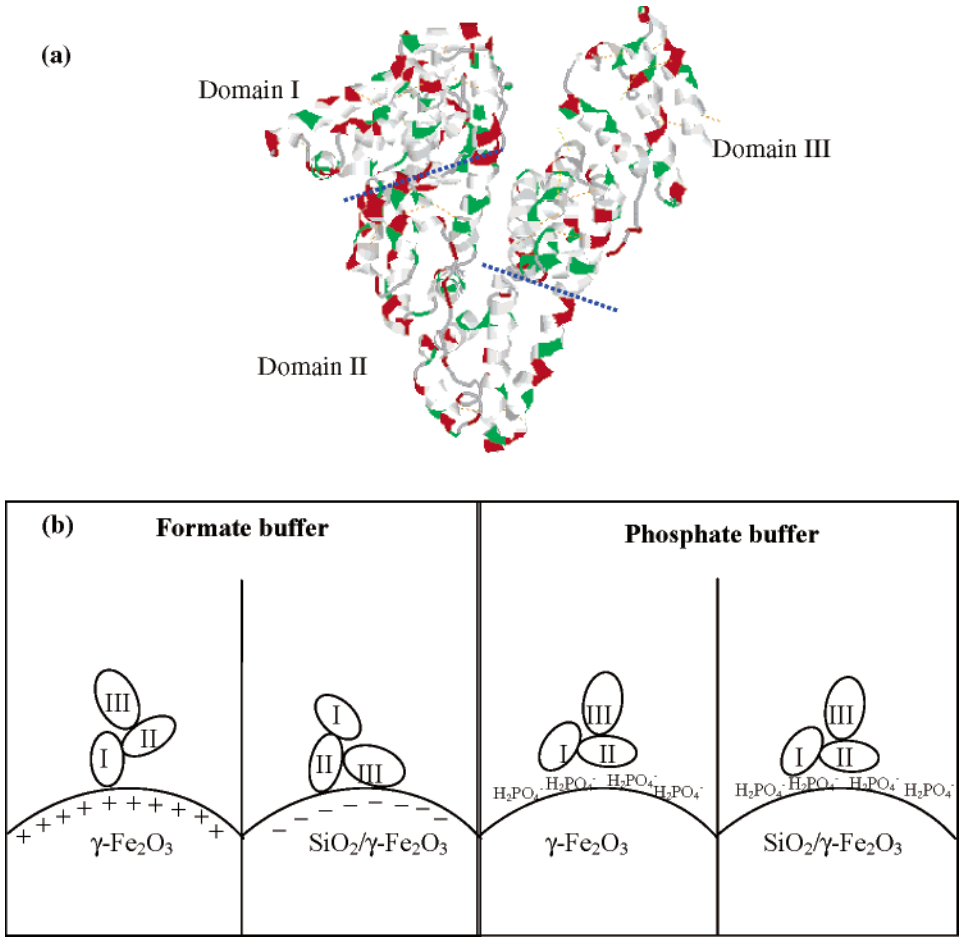

Figure 7. Illustration of (a) native structure of HSA (sharing 76% sequence identity with BSA, PDB code 1AO6) drawn with Protein Explorer: red and green regions represent acidic and basic amino acids, respectively, and (b) proposed BSA orientation during adsorption onto γ-Fe_2O_3 and SiO_2/γ-Fe_2O_3 particles.

the particles in phosphate buffer before BSA adsorption (Table 3). This is further confirmed by FT-IR analysis, where a distinct P═O characteristic peak at 1055 cm^{-1} could be seen (Figure 8b, iv). The specific adsorption of phosphate ion on iron oxide particles has been reported by many authors.[53−54] The general consensus is that the specific phosphate anion adsorption occurs via an exchange reaction with the hydroxyl group on the particle surface. Hence, phosphate anions could have served as bridging ligand between the hydroxyl group on the particle surface and the BSA molecules in the adsorption process and caused the altered orientation (Figure 7).

In both buffer systems, the adsorption saturation for sol−gel-coated SiO_2/γ-Fe_2O_3 was much lower than the value for FSP-synthesized particles, estimated to be approximately half the value predicted for monolayer coverage. Although the reason for such low adsorption is unknown at this stage, a possible cause was the higher degree of overall hydrophilicity arising from a better SiO_2 encapsulation in the sol−gel-coated SiO_2/γ-Fe_2O_3. Soft proteins such as BSA have been reported to adsorb on hydrophilic surfaces by structure rearrangement[55] such as expansion, unfolding, or different degrees of tilting upon adsorption. These rearrangements would alter the contact area that each BSA molecule occupied upon adsorption, and could be responsible for the lowered saturation adsorption value on sol−gel-coated SiO_2/γ-Fe_2O_3. Simple electrostatic interaction difference was ruled out as a cause for the decrease, since both FSP and sol−gel-coated SiO_2/γ-Fe_2O_3 particles were shown to have similar ζ-potentials (Figure 5). In fact, no significant difference in ζ-potential was observed for all SiO_2/γ-Fe_2O_3 particles in both formate and phosphate buffers before BSA adsorption (Table 3).

3.2.2. BSA Desorption Studies. BSA desorption was investigated by replacing the supernatant after adsorption with fresh buffer solution. No BSA desorption was detected in both phosphate and formate systems, signifying the high affinity of BSA toward the particle surfaces. BSA adsorbed on γ-Fe_2O_3 and SiO_2/γ-Fe_2O_3 particles was subsequently desorbed using two different techniques: by the addition of (1) KOH to formate system or K_2HPO_4 to phosphate system, both at pH 9.6, and (2) 1 M KCl dissolved in 10 mM of the respective buffer.

Addition of KOH (pH 9.6) onto recovered γ-Fe_2O_3 only managed to desorb about 40% of the BSA initially adsorbed in the formate buffer (Figure 9a). At that pH, the γ-Fe_2O_3 (IEP = 7.9, Figure 5) and all BSA domains (IEP = 4.7) would render highly negative charges and repel one another if they were only held by electrostatic forces. Nevertheless,

(53) Urano, H.; Fukuzaki, S. *J. Ferment. Bioeng.* **1997**, *83*, 261.
(54) Kouassi, G. K.; Irudayaraj, J.; McCarty, G. *BioMagn. Res. Technol.* **2005**, *3* (1), 1.
(55) Norde, W.; Giacomelli, C. E. *J. Biotechnol.* **2000**, *79*, 259.

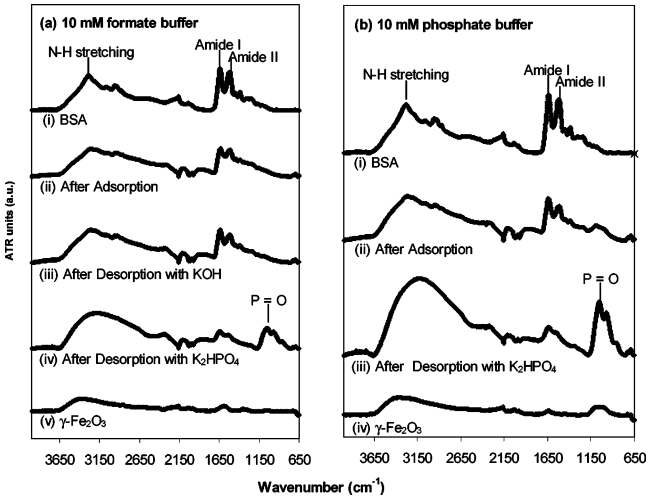

Figure 8. FT−IR spectra of BSA, fresh γ-Fe_2O_3 (d_{XRD} = 14 nm), after BSA adsorption, and after desorption in (a) formate and (b) phosphate systems.

the incomplete desorption at pH 9.6 could be due to the hydrophobic interaction between γ-Fe_2O_3 and BSA. This is consistent with the previous discussion that the high amount of BSA adsorbed in the formate buffer was partly attributed to the strong hydrophobic interaction. The nondesorbed BSA was clearly shown by the intense BSA FT-IR characteristic peaks (Figure 8a, iii). Similar observation was also noted by Peng et al.,[56] who also failed to desorb BSA effectively from magnetite particles using NaOH (pH 12.37). Interestingly, 90% of BSA desorption was achieved when K_2HPO_4 (pH 9.6) was used as the desorption agent. Phosphate ions, as evidenced earlier, have high affinity toward γ-Fe_2O_3 surface and thus would be able to displace most of the BSA. The strong P═O peak and nearly vanished BSA amide bands observed on the phosphate-desorbed particles under FT−IR (Figure 8a, iv) further confirm the postulation. Readsorption of BSA did not take place despite the presence of a phosphate bridging ligand due to strong electrostatic repulsion at pH 9.6. Desorption of BSA on FSP and sol−gel-coated SiO_2/γ-Fe_2O_3 by KOH (pH 9.6) addition was more effective (~70%, Figure 9a), probably due to a less significant hydrophobic attraction.

Increasing the ionic strength by the addition of 1 M KCl in formate buffer only yielded 20−30% BSA recovery for both γ-Fe_2O_3 and SiO_2/γ-Fe_2O_3 (Figure 9a). Although the increase in ionic strength should (1) promote the competition of salt ion with protein molecules in occupying adsorption sites and (2) offset the electrostatic particle−BSA interaction by binding to ionized groups on BSA molecules,[57] the choice of foreign ions proved to be an important factor to take into consideration. The presence of Cl^- in this case failed to interact specifically with the particle surface and/or surface-bound BSA.

Desorption of previously adsorbed BSA in phosphate buffer with K_2HPO_4 (pH 9.6) was found to be effective for both γ-Fe_2O_3 and SiO_2/γ-Fe_2O_3 samples, with a recovery of >70% (Figure 9b). The γ-Fe_2O_3 surface after desorption with

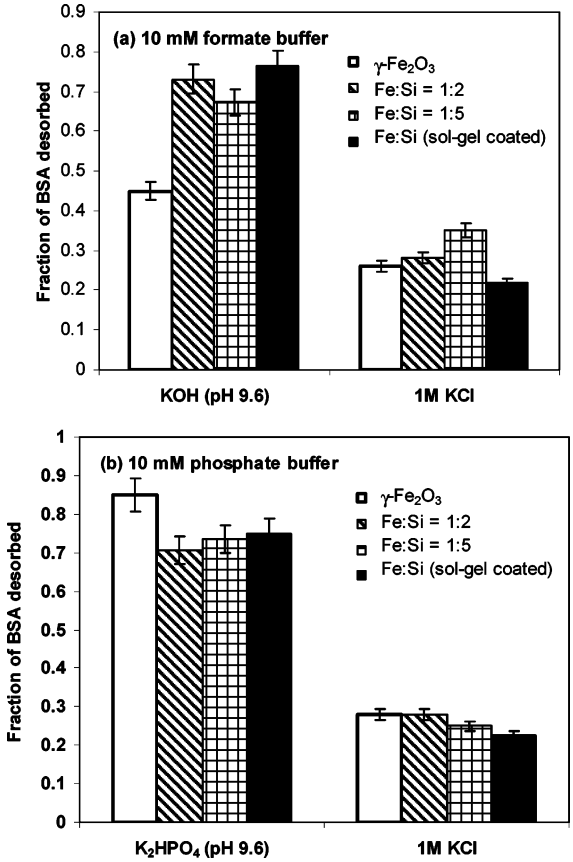

Figure 9. Fraction of BSA desorbed from γ-Fe_2O_3 and SiO_2/γ-Fe_2O_3 in (a) formate and (b) phosphate systems at pH 9.6 by addition of KOH and K_2HPO_4 respectively, and also by addition of 1 M KCl.

K_2HPO_4 in phosphate buffer (Figure 8b, iii) had a similar FT−IR spectrum as that of the same particle after K_2HPO_4 desorption in the formate system (Figure 8a, iv). In addition, the ζ-potentials of γ-Fe_2O_3 after desorption for both cases were similar. The observation implied that, by using K_2HPO_4 as desorbing agent, the γ-Fe_2O_3 particle surface became identical in both systems after desorption. It is interesting to note that the phosphate ions (P═O peak), which were previously used as bridging ligand, were now readily observed when BSA is desorbed (Figure 8b, iii).

Similar to formate buffer, desorption by increasing the ionic strength through the addition of 1 M KCl in phosphate buffer was inefficient and only yielded <30% desorption (Figure 9b). Avramescu et al. carried out similar desorption studies for BSA adsorbed at pH 4.5 onto a polymeric matrix using acetate buffer with 1 M NaCl and found that the adsorbed BSA could not be desorbed by a gradient of salt concentration or an increase of ionic strength.[57]

4. Conclusion

A direct (one-step) FSP technique was used to produce predominantly room-temperature superparamagnetic γ-Fe_2O_3 and SiO_2/γ-Fe_2O_3 nanoparticles with closely controlled properties. The as-prepared γ-Fe_2O_3 samples with d_{XRD} of 6, 14, and 21 nm were of hexagonal platelet-shaped structure with high surface area and nonporous surface. A decrease in saturation magnetization, σ_s from 74 to 21 emu/g of γ-Fe_2O_3 was observed with decreasing particle size. Two

(56) Peng, Z. G.; Hidajat, K.; Uddin, M. S. *Colloids Surf. B* **2004**, *33*, 15.
(57) Avramescu, M-E.; Girones, M.; Borneman, Z.; Wessling, M. *J. Membr. Sci.* **2003**, *218*, 219.

distinct SiO_2/γ-Fe_2O_3 morphologies, both nonporous, could be obtained by varying the Fe:Si ratio to 1:2 and 1:5. A visibly segregated γ-Fe_2O_3 core to the edge of every SiO_2 particle could be observed in the former, while well-dispersed γ-Fe_2O_3 multicores embedded in spherical SiO_2 were obtained in the latter. The σ_s value was $\sim 39 \pm 1$ emu/g of γ-Fe_2O_3 for both coated samples. Coating of SiO_2 on γ-Fe_2O_3 ($d_{XRD} = 14$ nm) by sol−gel resulted in a continuous thin layer around a few particles. The particles were nonporous with σ_s of 53 emu/g of γ-Fe_2O_3. Both the FSP and sol−gel-coated SiO_2/γ-Fe_2O_3 samples exhibited similar ζ-potential profile. However, acid dissolution studies showed better SiO_2 encapsulation for the sol−gel-coated particles.

Adsorption of BSA was carried out on 14-nm γ-Fe_2O_3 and all SiO_2/γ-Fe_2O_3 samples (Fe:Si = 1:2, 1:5, and sol−gel-coated) in both 10 mM formate and phosphate buffers at pH 5.3. In all cases, BSA adsorption could be described by a simple Langmuir isotherm. Except for BSA adsorption on γ-Fe_2O_3 in formate buffer, which followed an end-on conformation, all the other samples were found to obey the side-on adsorption model. All FSP-made particles showed saturation adsorption capacity close to the theoretical limit. Sol−gel-coated SiO_2/γ-Fe_2O_3 only showed an adsorption capacity approximately half of the theoretical side-on limit, presumably due to the more complete encapsulation of hydrophilic SiO_2. In the formate system, BSA could be effectively desorbed at pH 9.6 for all SiO_2/γ-Fe_2O_3 particles, due to the electrostatic repulsion between BSA and the particles. However, the interaction between BSA and γ-Fe_2O_3 particle surface could not be easily overcome simply by changing the pH. Addition of phosphate ion was necessary to displace BSA from γ-Fe_2O_3 surface. Accordingly, desorption of BSA on all particles could be easily achieved at pH 9.6 in phosphate buffer. Increasing ionic strength through 1 M KCl addition only yielded <30% desorption.

Although the FSP-synthesized SiO_2/γ-Fe_2O_3 particles had lower saturation magnetism, in this case, their BSA binding capacity was observed to be twice that obtainable on the conventional sol−gel-prepared counterpart. Both of these factors need to be taken into consideration when choosing a suitable carrier for protein separation.

Acknowledgment. The authors thank Professor S. E. Pratsinis (ETH Zürich) and Dr. L. Mädler (UCLA) for FSP reactor design and setup. This work was produced with the financial assistance of the Australian Research Council under the ARC Centres of Excellence Program.

Supporting Information Available: XRD, TEM, N_2 adsorption, SQUID, ζ-potential, and protein adsorption−desorption procedure. This material is available free of charge via the Internet at http://pubs.acs.org.

CM061861V